Pressure-Induced Topological Non-Trivial Phase and Tunable Optical Properties in All-Inorganic Halide Perovskites

Yiran Ying, Xin Luo*, and Haitao Huang*

Department of Applied Physics, The Hong Kong Polytechnic University, Hung Hom, Kowloon,

Hong Kong, P.R. China

ABSTRACT. Cesium-based all-inorganic halide perovskites $CsMX_3$ (M=Pb, Sn; X=Cl, Br, I) have been considered as an important candidate for highly-efficient, chemically stable optoelectronic devices and solar cells. Pressure can serve as an effective and clean thermodynamic approach to better performance of $CsMX_3$. In this work, we use first-principles density functional theory calculations with both PBE and GW+BSE to systematically study the effects of pressure

on the electronic structures, carrier transport and optical properties of cubic phase $CsMX_3$. Our results show that with increasing hydrostatic pressure, the optical band gap red-shifts until the pressure reaches a critical value, above which the band inversion was observed due to the spin-orbit coupling. The resulting non-trivial topological gap blue-shifts with further increasing pressure. This work provides insights into the rational design of experiments to engineer properties of $CsMX_3$ perovskites by applying pressure.

TEXT.

INTRODUCTION

Metal halide perovskites (MHPs) have emerged as promising candidates for high-efficiency optoelectronic devices and solar cells owing to their preeminent electronic and optical properties.[1-3] In the past several years, the power conversion efficiency of MHP-based solar cells has experienced a conspicuous increase from 9.7% in 2012[4] to 22.1% in 2017[5]. From the perspective of materials, MHPs have the general formula of AMX_3, where A is a monovalent cation (inorganic Cs^+, organic FA^+ and MA^+), M is a divalent metal cation (Sn^{2+}, Pb^{2+}) and X is a halogen atom (Cl^-, Br^-, I^-)[1]. Among the family of MHPs, organic-inorganic hybrid lead halide perovskites $MAPbX_3$ and $FAPbX_3$ exhibit high energy conversion efficiencies.[5-8] However, their bottlenecks lie in long-term chemical instability. Recently, a study by Kulbak *et al.* has shown that cesium-based all-inorganic halide lead perovskites $CsPbX_3$ have higher stability than organic-inorganic hybrid perovskites with comparable photoelectric performance.[9] Moreover, $CsPbX_3$ are less soluble in common solvents than $MAPbX_3$[10], which makes it more convenient to obtain nanocrystal (NC)

CsPbX$_3$ quantum dots with high photoluminescence quantum yield.[10-12] Therefore, CsPbX$_3$ perovskites NCs have been extensively examined for their potential applications in light-emitting diodes[12-14], lasing materials[15-16], *etc*. In addition, an alternative lead-free, non-toxic all-inorganic MHPs CsSnX$_3$ NCs were also synthesized and reported with tunable optical properties[17]. Nevertheless, developing an efficient way to engineer the properties of MHPs still remains a critical question in designing optoelectronic devices and solar cells with even higher efficiency and stability.

Compared to modifying chemical reaction steps and compounds[18-21], applying pressure has been considered as a green and facile strategy to regulate the structure and properties of organic-inorganic hybrid MHPs[22-26] as well as all-inorganic MHPs[27-28]. The exertion of pressure by a diamond anvil cell (DAC) is commonly used in experiments to reduce distances between atoms and lead to a closer packing, which would regulate orbitals and electronic properties of MHPs. For example, experiments revealed that MHP-based CsPbBr$_3$ NCs have a narrower band gap and prolonged carrier lifetime at high pressure.[27] According to Zhang *et al.*, CsPbBr$_3$ structure exhibits an isostructural phase transition at around 1.2 GPa, which leads to the band gap red shifting before 1.0 GPa, followed by blue shifting when the pressure is during 1.0-2.0 GPa.[28] The tunable electronic and optical properties of the orthorhombic CsPbBr$_3$ in aforementioned work are attributed to Pb-Br bond length shrinkage and PbBr$_6$ octahedral distortion under high pressure. Recently, Yuan *et al.* reported a phase transition of orthorhombic phase CsPbI$_3$ under a pressure of around 3.9 GPa.[29] Nevertheless, the high-temperature cubic CsMX$_3$ (M=Pb, Sn; X=Cl, Br, I) perovskites, which have narrower band gap than their orthorhombic counterparts and are predicted to have intriguing physics such as 3D topological insulators,[30] have not yet been fully explored under high pressure.

Herein, by applying first-principles density functional theory (DFT) in both generalized gradient approximation and many body quasi-particle (GW) calculations, we systematically examine the pressure engineering on the elastic, electronic, carrier transport, and optical properties of cubic cesium-based all-inorganic perovskites $CsMX_3$ (M=Pb, Sn; X=Cl, Br, I). The effects of spin-orbit coupling (SOC) have also been discussed. This work provides predictive insights into guiding the judicious design of experiments to optimize the electronic and optical properties of MHPs by introducing pressure to improve the performance of optoelectronic devices.

COMPUTATIONAL METHODS

Density functional theory (DFT) calculations were performed using Vienna *ab initio* simulation package (VASP)[31-32] version 5.4.4 with wave functions described by a plane-wave basis set and projector-augmented wave (PAW) potentials[33]. For Cs, Pb, Sn, Cl, Br, and I, $5s5p6s$, $5d6s6p$, $4d5s5p$, $3s3p$, $4s4p$, and $5s5p$ electrons were treated as valence electrons, respectively. For the exchange and correlation functional, local density approximation (LDA), generalized gradient approximation (GGA) with Perdew-Burke-Ernzerhof parametrization (PBE)[34], PBE revised for solids (PBEsol)[35], strongly constrained and approximately normed meta-GGA with revised Vydrov-Van Voorhis non-local density functional (SCAN+rVV10)[36] were tested for lattice constants during geometric optimization. Energy cutoff for the plane wave basis was set as 450 eV for all calculations and the *k*-points sampling with a Monkhorst-Pack mesh[37] was set as 5×5×5, which can lead to sufficiently converged total energy for $CsMX_3$ in one unit cell based on the results of convergence test (Figure S1 and S2). The atomic positions were allowed to relax until energy was less than 1×10^{-7} eV and the absolute value of force on the atom was less than 0.01 eV/Å.

Finite distortions of the lattices along each Cartesian directions are calculated to obtain Hessian matrices and we use the strain-stress relationship to derive elastic constants out of them afterwards.[38] As for cubic phase $CsMX_3$, only three elastic constants C_{11}, C_{44} and C_{12} are independent, and we can compute bulk modulus K, shear modulus G, Young's modulus E and Poisson ratio υ out of them using the following formula[39-40]:

$$K = \frac{C_{11} + 2C_{12}}{3}$$

$$G = \frac{5C_{44}(C_{11} - C_{12})}{8C_{44} + 6(C_{11} - C_{12})} + \frac{C_{11} - C_{12} + 3C_{44}}{10}$$

$$\upsilon = \frac{3K - 2G}{6K + 2G}$$

$$E = 2G(1 + \upsilon)$$

Electron and hole effective masses m_e and m_h were obtained using the formula:

$$m_e = [\frac{1}{\hbar^2}\frac{\partial^2 E_{CBM}(k)}{\partial k^2}]^{-1}$$

$$m_h = [\frac{1}{\hbar^2}\frac{\partial^2 E_{VBM}(k)}{\partial k^2}]^{-1}$$

where $E_{VBM}(k)$ and $E_{CBM}(k)$ represent energy band of valence band maximum (VBM) and conduction band minimum (CBM), respectively.

Static dielectric tensors caused by electronic polarization ε_{std} as well as Bohn effective charges were calculated using density functional perturbation theory (DFPT). The exciton binding energies E_b were subsequently calculated using conventional Wannier-Mott hydrogenic model[41]:

$$E_b = \frac{m_e m_h}{m_0(m_e + m_{h)}} \cdot \frac{R_y}{\varepsilon_{std}^2}$$

where m_0 denotes electron rest mass, R_y=13.6057 eV is the Rydberg energy constant. Electron and hole mobilities were calculated using deformation potential theory[42] with the following forms:

$$\mu_e = \frac{2\sqrt{2\pi}e\hbar^4 K}{3E_1^2(k_B T)^{3/2}m_e^{5/2}}$$

$$\mu_h = \frac{2\sqrt{2\pi}e\hbar^4 K}{3E_1'^2(k_B T)^{3/2}m_h^{5/2}}$$

where $E_1 = \frac{dE(VBM)}{d\delta}$ and $E_1' = \frac{dE(CBM)}{d\delta}$ are the deformation potential, dE(VBM), dE(CBM) and dδ denote energy of VBM, energy of CBM, and lattice constant changes due to small hydrostatic pressure, respectively.

For the optical property calculations, the excitonic effect was included through solving the Bethe-Salpeter equation (BSE)[43-44] with Tamm-Dancoff approximation[45] on top of single-shot G_0W_0. For comparison, random phase approximation (RPA)[46] was also applied. Gamma-centered 6×6×6 grid was used for k-points sampling during GW and BSE calculations. Absorption coefficient α(ω) and reflectivity R(ω) were given by the following equations:

$$\alpha(\omega) = \sqrt{2}\omega[\sqrt{\varepsilon_1(\omega)^2 + \varepsilon_2(\omega)^2} - \varepsilon_1(\omega)]^{1/2}$$

$$R(\omega) = |\frac{\sqrt{\varepsilon_1(\omega) + i\varepsilon_2(\omega)} - 1}{\sqrt{\varepsilon_1(\omega) + i\varepsilon_2(\omega)} + 1}|^2$$

where $\varepsilon_1(\omega)$ and $\varepsilon_2(\omega)$ represent real and imaginary parts of frequency-dependent dielectric function, respectively. Due to computational limits, spin-orbit coupling effect was included by adding the scissor correction obtained from PBE calculations to the final non-SOC GW calculations.

RESULTS AND DISCUSSION

Typical crystal structure of cubic CsMX$_3$ (M=Pb, Sn; X=Cl, Br, I) with space group *Pm-3m* is shown in Fig. 1(a). Naturally, the effects of hydrostatic pressure on crystal structure and properties are directly reflected in the evolution of lattice constants. The relaxed lattice constants *a* for cubic CsMX$_3$ and experimental values under zero pressure calculated using different functionals are

listed in Table S1. PBEsol functional outperforms LDA, PBE, and SCAN+rVV10 when predicting

lattice constants, giving a mean error of 0.72% compared to experimentally measured data, which

is in accordance with previous functional assessment results about lattice constants for solids[47]. By

applying hydrostatic pressure up to 8 GPa during DFT calculation, theoretical lattice constants as

a function of pressure are obtained and plotted in Figure S3. The lattice constants have a decreasing

trend with increasing pressure for all six systems while no distortions of MX_6 octahedra are found,

which can be attributed to the contraction of MX_6 octahedra and shrinkage of M-X bond length.

The totally relaxed structures using PBEsol functional are used as initial structures in the following
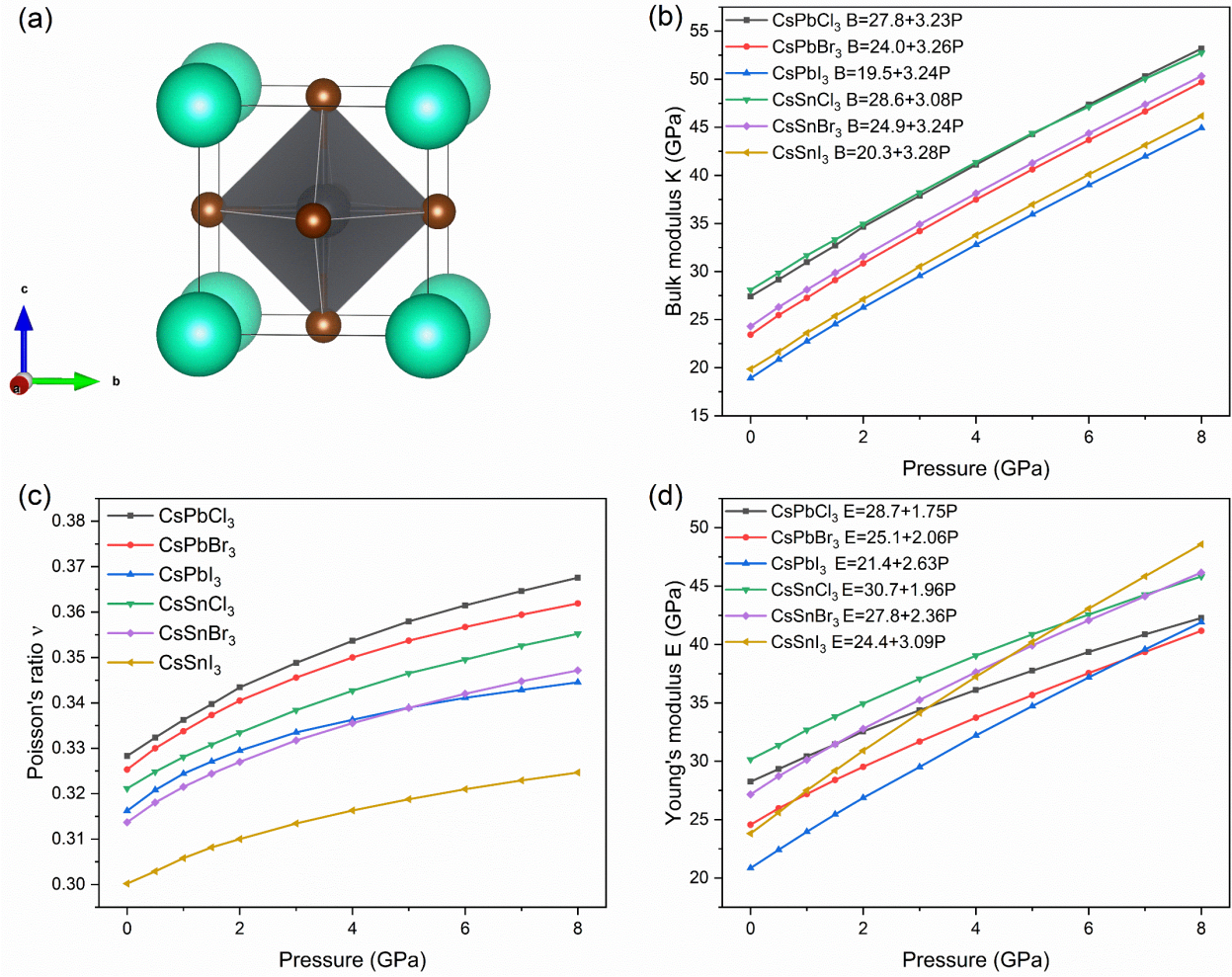
calculations.

Figure 1. (a) Schematic crystal structure of cubic CsMX$_3$ (Green: Cs; Black: M; Brown: X). (b) Bulk moduli K, (c) Poisson's ratios v, and (d) Young's moduli E of cubic phase CsMX$_3$ as a function of pressure P. For K-P and E-P relationships, linear fitting results for the different moduli are also shown in the figures.

Next, we endeavor to determine the influence of pressure on the elastic constants. The values of bulk modulus K, shear modulus G, Young's modulus E, and Poisson ratio v under pressure for CsMX$_3$ are shown in Figure 1(b)-(d) and S4. For all elastic properties, an increasing trend with pressure going up to 8 GPa can be found. M-X bond length reduction under pressure is the main

8

reason for elastic properties modification and a closer packing can lead to higher stiffness of materials. For bulk moduli K, the general trends for systems under no pressure are Sn>Pb and Cl>Br>I and these trends remain when the pressure is increased up to 8 GPa. For shear moduli G and Young's moduli E, however, iodine-based systems $CsSnI_3$ and $CsPbI_3$ are more sensitive to pressure than bromine- and chlorine-based systems, giving larger slopes of G-P and E-P fitting lines.

As for electronic properties, we start by examining band structures of $CsMX_3$ systems under 0, 2, and 5 GPa calculated using PBE (Figure S5). The fact that cubic $CsMX_3$ show semiconducting behavior with the direct band gap at R point is in agreement with previous work[48]. Nevertheless, when the pressure is increased to 2 GPa and finally 5 GPa, the direct band gap at R point suffers a declining tendency for all cubic $CsMX_3$ systems. Band gap evolution under PBE level is plotted in Figure S6(a). To get a better view of orbital occupancies around Fermi energy level and determine the contributions of separate elements and orbitals, we plot density of states (DOSs) under pressure of 0 and 2 GPa in Figure S7. Valence band maximum (VBM) can be identified as antibonding hybridization between X p and a small portion of M s orbitals while conduction band minimum (CBM) is mainly composed of M p and a small portion of X s orbitals (M=Pb, Sn; X=Cl, Br, I). We can see that orbitals of Cs have almost no contribution to DOSs around Fermi energy level and Cs cation is chemically inert, indicating that key contribution of the band gap in $CsMX_3$ is from the MX_6 octahedral network. Upon applying pressure, the shrinkage of M-X bond length results in an augmented coupling between M and X orbitals and decreased band gap values. Moreover, as shown in Figure S6(b), band gap reduction can be owed to the shifting of both CBM and VBM, while CBM is more sensitive to pressure (or M-X bond length) because of its dominant non-bonding localized M p orbital characteristics.

Since spin-orbit coupling (SOC) plays a significant role in determining exact values of the band gap of Pb-based MHPs[49], we further examine the band structures calculated using PBE+SOC. The band gap corrections due to SOC (Δ_{SOC}) under no pressure are listed in Table 1. Comparing to PBE results, including SOC in the calculation decreases the band gap for $CsMX_3$ systems except for the case of $CsSnI_3$, in which a slight increase of 0.11 eV is predicted. We plot the projected band structures of cubic $CsMX_3$ with SOC in Figure 2 and S8. For all structures, under hydrostatic pressure higher than critical values, in contrast to band structures without SOC, inversion of Pb/Sn s and p characteristic band structures and reopening of band gap can be observed. Band gap values under PBE+SOC as a function of pressure are shown in Figure 3(a). The observed band inversion in $CsPbCl_3$, $CsPbBr_3$, $CsPbI_3$, and $CsSnCl_3$ can be attributed to novel three-dimensional non-trivial topological insulating phases in $CsMX_3$ MHPs represented by isotropic Dirac fermions when SOC is introduced to the system. As illustrated in Figure S9, when SOC is considered, $|l=1>\otimes|s=1/2>$ states (Pb/Sn-p) governing CBM features are split into $|l=1,s=1/2,j=3/2>$ and $|l=1,s=1/2,j=1/2>$ states. The latter ones interact with $|l=0,s=1/2,j=1/2>$ states (Pb/Sn-s) which govern VBM features and form the non-degenerate bands with the only exception of Kramers degeneracy for half-integer total spin[50]. The non-degeneracy results in non-trivial band topology and inversion of conduction and valence bands with reduced lattice parameters in the systems induced by moderate hydrostatic pressure. Critical pressure values of trivial to non-trivial band topology transition are located at 6.0 GPa, 2.5 GPa, 0.7 GPa, 1.6 GPa for $CsPbCl_3$, $CsPbBr_3$, $CsPbI_3$ and $CsSnCl_3$, respectively, under which gapless Dirac cones can be noticed (Figure 2). On the other hand, $CsSnBr_3$ and $CsSnI_3$ have non-trivial band gap even under zero pressure (Figure S8(c) and S8(d)). Above critical pressure, the blue-shifting of electronic band gap is predicted. In the proximity of topological trivial to non-trivial phase transition, small changes in lattice constants can robustly result in

reversed photocurrent directions, sharpened current peaks and improved intensities.[51] Such change of current response in topological non-trivial phase and band inversion may suggest a novel way to enhance the bulk photovoltaic effect of MHPs for light-harvesting applications.

Table 1. Experimental band gap values (eV) and those calculated using PBE, PBE+SOC, G_0W_0, GW_0, and GW_0+SOC of cubic $CsMX_3$ (M=Pb, Sn; X=Cl, Br, I) under zero pressure.

System	$CsPbCl_3$	$CsPbBr_3$	$CsPbI_3$	$CsSnCl_3$	$CsSnBr_3$	$CsSnI_3$
PBE	1.96 (-0.89)	1.54 (-0.82)	1.26 (-0.41)	0.64 (-1.96)	0.27 (-1.48)	0.13 (-1.17)
PBE+SOC	0.88 (-1.97)	0.46 (-1.90)	0.15 (-1.52)	0.31 (-2.29)	0.06 (-1.69)	0.24 (-1.06)
Δ_{SOC}	-1.08	-1.08	-1.11	-0.33	-0.21	0.11
G_0W_0	3.20 (0.35)	2.50 (0.14)	1.99 (0.32)	1.41 (-1.19)	0.81 (-0.94)	0.56 (-0.74)
GW_0	3.67 (0.82)	2.88 (0.52)	2.25 (0.58)	1.73 (-0.81)	1.02 (-0.73)	0.69 (-0.61)
GW_0+SOC	2.59 (-0.26)	1.80 (-0.56)	1.14 (-0.53)	1.40 (-1.20)	0.81 (-0.94)	0.80 (-0.50)
Exp.	2.85[a]	2.36[b]	1.67[c]	~2.60[d]	1.75[e]	1.30[c]
Δ_T	0.50	0.39	0.47	0.62	0.64	0.64

Experimental values come from: (a) Ref 52; (b) Ref 9; (c) Ref 53; (d) Ref 17; (e) Ref 54. The differences between calculated and experimental values are listed in parenthesis. Band gap opening values due to finite temperature Δ_T are extracted from Ref 55.
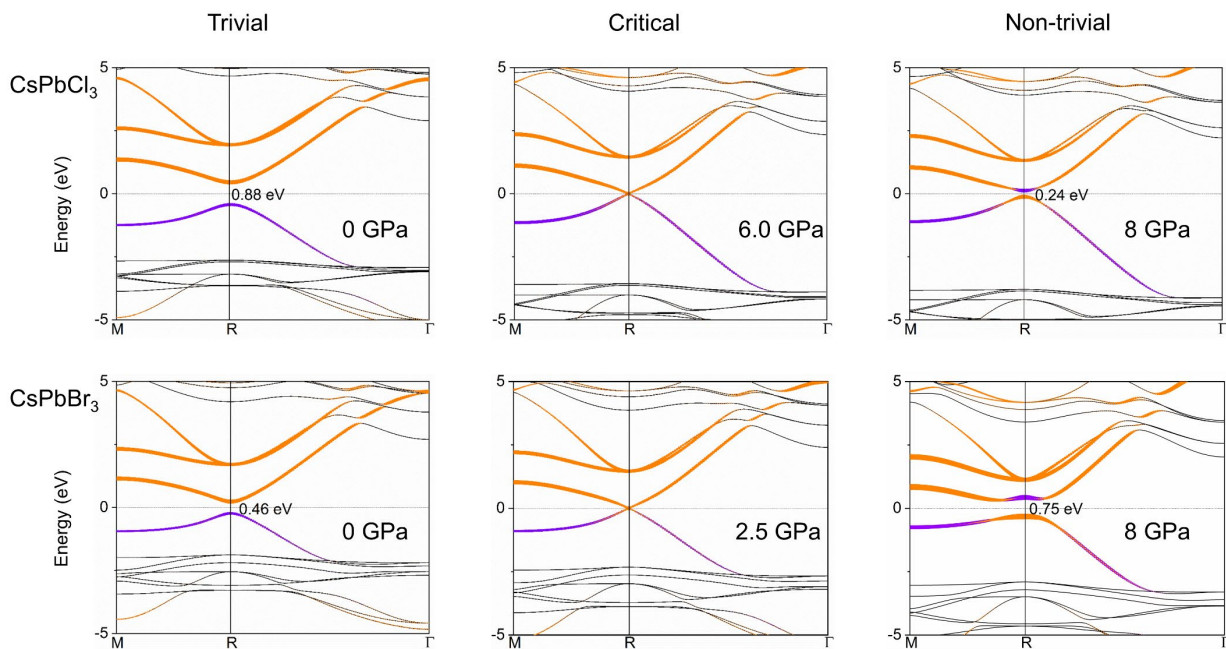
Figure 2. Characteristic band structures of cubic phases of CsPbCl$_3$ and CsPbBr$_3$ under trivial, critical, and non-trivial pressure conditions calculated using PBE+SOC. Dotted lines denote Fermi energy levels. The sizes of the purple and orange dots in the figure are proportional to the weights of the projections of the *s* and *p* states onto Pb atom, respectively.
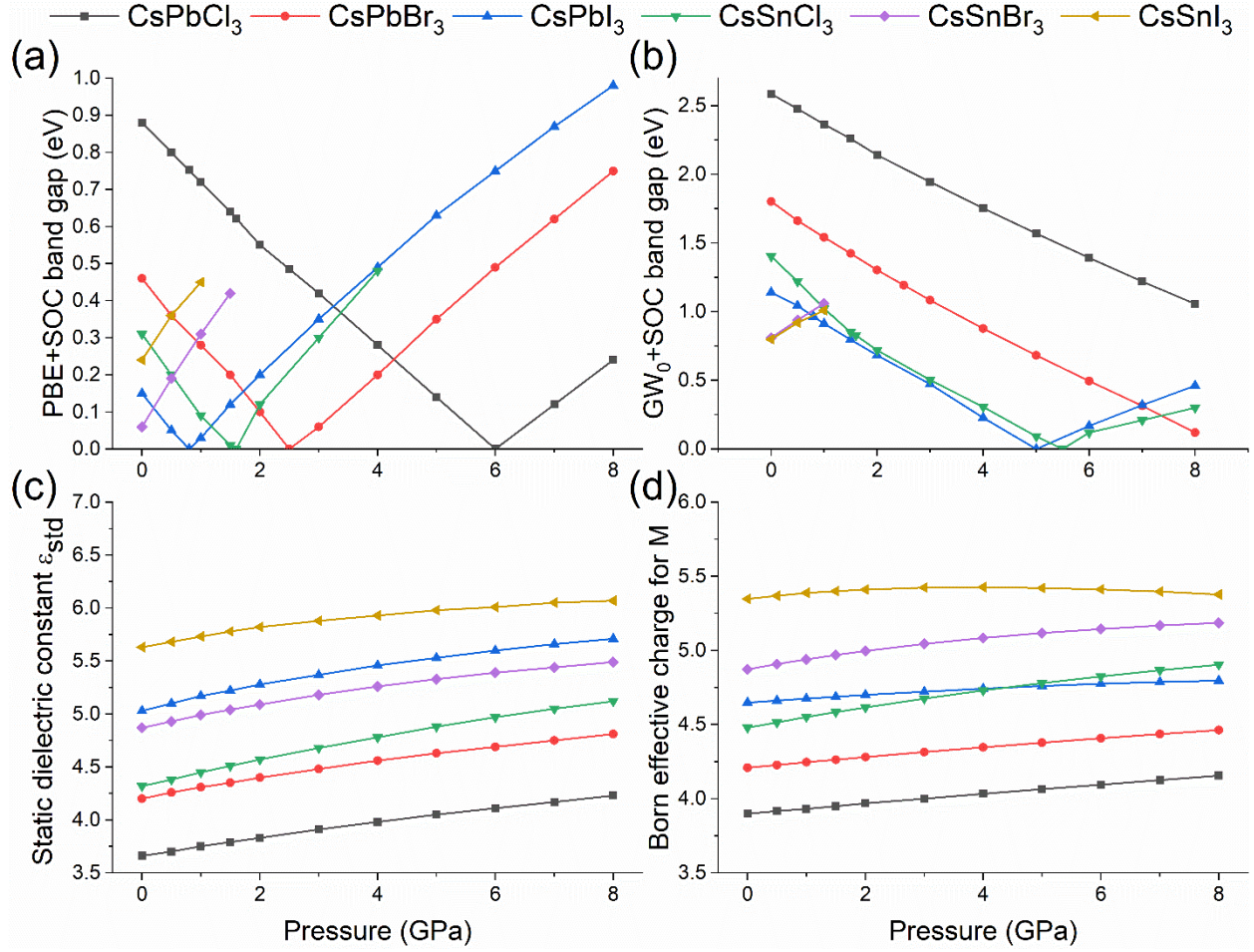
Figure 3. (a) PBE+SOC and (b) GW_0+SOC electronic band gap values, (c) static dielectric constants, and (d) Born effective charges for M (M=Pb, Sn) of cubic phase $CsMX_3$ as a function of pressure.

PBE is known for its underestimation of exact band gap values.[56] In order to get more rigorous values of band gap for $CsMX_3$, we apply many-body perturbation theory with GW approximation, which includes many-body electron-electron interaction, to predict the accurate band gap[57-58] for $CsMX_3$. Two levels of GW calculations are used: (a) single-shot quasiparticle GW (G_0W_0); (b) partial self-consistent quasiparticle GW (GW_0). Convergence test results show that the number of the unoccupied band of 512 is sufficient enough in GW calculations since reducing it to 256 gives band gap values with the error less than 0.01%. Band gap values at R point as a function of pressure

13

for $CsMX_3$ at GW_0 level are plotted in Figure S6(c). Similar to PBE calculations, the band gap tends to red-shift with increasing pressure. Band gap values E_g under zero pressure calculated using PBE, G_0W_0, GW_0 and measured by experiments are listed in Table 1. At the same time, since SOC is not included in GW calculations, we use the SOC correction Δ_{SOC} calculated from PBE to get GW_0+SOC results E_g (GW_0+SOC) (see Figure 3(b), Figure S6(d), and notes below Figure S6 for more details about band gap correction under pressure). Relatively smaller E_g (GW_0+SOC) values for the $CsMX_3$ systems compared to experiments under zero pressure (see Table 1) are attributable to the neglect of thermal effects in DFT calculations. As discussed in a recent work combining the rVV10 functional calculation with molecular dynamics simulations, the band gap will have increments Δ_T ranging from 0.39 to 0.64 eV due to finite temperature[55] (listed in Table 1), with which we can obtain more realistic band gap values. This can be ascribed to the thermal expansion effect that gives rise to the lattice parameters and the spontaneous octahedral tilting of $CsMX_3$.

It is suggested that carrier transport properties in halide perovskites can be benefited by large Born effective charges and dielectric constants.[59] Here, we use density functional perturbation theory to study the dielectric properties as a function of pressure. Note that dielectric constants as well as Born effective charges (Z^*) for cubic $CsMX_3$ are isotropic so we only focus on xx components. Static dielectric constants ε_{std} under zero pressure are listed in Table 2. We then derive the electron and hole effective masses of $CsMX_3$ along high symmetry directions R->Γ near the band gap edge from PBE+SOC band structures calculations. Electron and hole mobilities μ_e and μ_h under 300 K are thus calculated. Through further calculations, we can expect both ε_{std} and Z^* for Pb/Sn to have larger values with increasing pressure for $CsMX_3$ with the only exception of Z^* for Sn in $CsSnI_3$, which decreases slightly after the pressure exceeds 5 GPa (Figure 3(c) and 3(d)).

Generally speaking, pressure can serve as an effective approach toward better carrier transport properties and enhanced screening effect of carriers from impurity centers, leading to better performance of MHP-based devices.

Table 2. PBE+SOC calculated electron (m_e) and hole (m_h) effective masses, dielectric constants (ε_{std}), Born effective charges for Pb/Sn (Z^*), electron (μ_e) and hole mobilities (μ_h), and exciton binding energies (E_b) calculated using Wannier-Mott (WM) model under 300 K and zero pressure of cubic $CsMX_3$ (M=Pb, Sn; X=Cl, Br, I).

System	$CsPbCl_3$	$CsPbBr_3$	$CsPbI_3$	$CsSnCl_3$	$CsSnBr_3$	$CsSnI_3$
m_e/m_0	0.37	0.34	0.27	0.44	0.25	0.24
m_h/m_0	0.28	0.21	0.21	0.47	0.44	0.27
ε_{std}	3.66	4.20	5.03	4.32	4.87	5.63
Z^*	3.90	4.21	4.65	4.48	4.87	5.35
μ_e (10^2 cm^2/(V·s))	2.7	4.2	4.3	2.9	4.0	4.0
μ_h (10^2 cm^2/(V·s))	8.6	27.1	28.2	1.6	2.6	8.8
E_b (meV)	162.42	99.78	63.19	165.72	91.79	55.36

Optical properties of $CsMX_3$ are also examined using DFT. Due to the cubic symmetry of $CsMX_3$, dielectric tensor $\varepsilon(\omega)=\varepsilon_1(\omega)+i\varepsilon_2(\omega)$ has only identical xx, yy, and zz components. We take the average of $\varepsilon_{xx}(\omega)$, $\varepsilon_{yy}(\omega)$ and $\varepsilon_{zz}(\omega)$ in the following calculations. The excitonic effect has been proven to be of vital importance in calculating optical properties of MHPs and calculations considering excitonic effect can provide better agreement with experiments.[60-61] We incorporate many-electron interactions and excitonic effects by solving the Bethe-Salpeter equation (BSE)

based on single-shot G_0W_0 and get the imaginary part of ground-state dielectric function $\varepsilon_2(\omega)$ (Figure S10). For comparison, results from random phase approximation (RPA) based on G_0W_0 are also presented. We note that including excitonic effects considerably reshapes the curves and GW+BSE results show smaller photon energy and higher intensities of $\varepsilon_2(\omega)$ for the first peak. On the basis of frequency-dependent dielectric functions calculated using G_0W_0+BSE, we plot the absorption spectra $\alpha(\omega)$ and reflectivity $R(\omega)$ in Figure 4, S11, and S12. We can identify the optical absorption peaks corresponding to direct transition at R point in the band structures and mark the peak positions in Figure 4. When the pressure is increased, the peak intensities are decreased indicating weaker exciton transitions. In addition, the trend of significant red-shifting with increasing pressure can be observed for all the systems, which is consistent with the preceding electronic band gap evolution results in Figure S6. Exciton binding energies are calculated through conventional Wannier-Mott (WM) hydrogenic model and the results under zero pressure are listed in Table 2. Direct subtraction of G_0W_0+BSE optical band gap from G_0W_0-calculated electronic band gap can give E_b values with the same order of magnitude, confirming the validity of WM model for the $CsMX_3$ systems. The decreasing trend of E_b from Cl to Br and finally to I can be also observed, indicating that faster photon-induced carrier dissociation can be achieved in iodine-based systems.
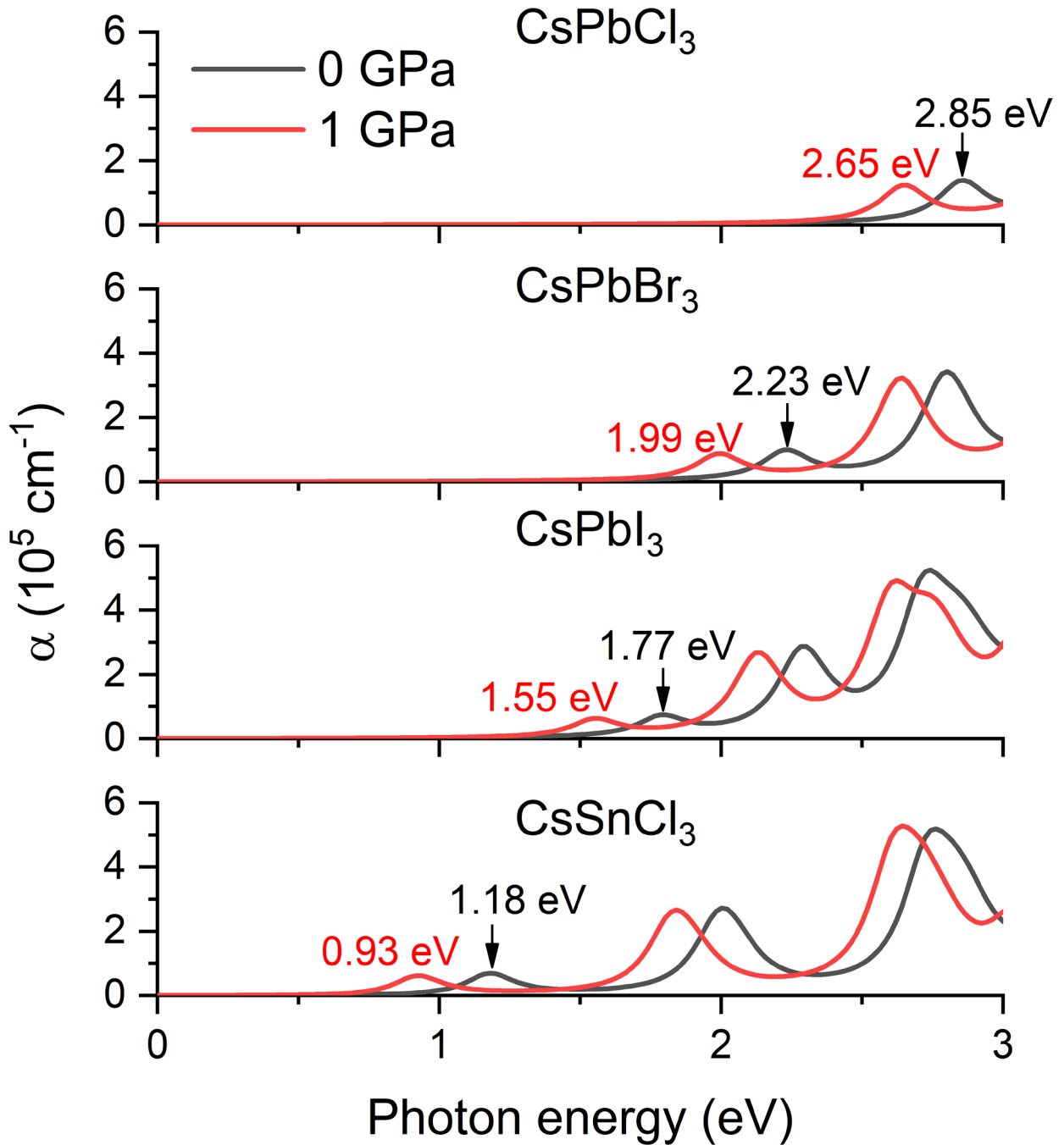
Figure 4. Pressure-dependent absorption spectra $\alpha(\omega)$ of cubic phases of $CsPbCl_3$, $CsPbBr_3$, $CsPbI_3$, and $CsSnCl_3$ calculated using GW+BSE. Positions of the first peak of the absorption spectra are marked in the figures.

CONCLUSION

In summary, elastic, electronic, carrier transport, and optical properties of cubic phase CsMX$_3$ with hydrostatic pressure applied have been investigated using density functional theory in this work. PBE and GW+BSE levels of calculations were both applied to come to the conclusion that applying appropriate hydrostatic pressure can lead to band gap red-shifting. Higher stiffness and enhanced carrier mobilities are obtained by pressure engineering for CsMX$_3$. In addition, three-dimensional topological non-trivial phase, band inversion, and blue-shifting above critical pressure can be also observed when the spin-orbit coupling is considered, resulting in large tunable optical properties. This work provides predictive evidence in experimental study of pressure-induced electronic and optical properties engineering. The strategies provided in this work are applicable to property studies of other kinds of perovskites and even other kinds of materials for designing devices with better optoelectronic and photovoltaic performance.

ASSOCIATED CONTENT

Supporting Information.

The following files are available free of charge.

Optimized lattice constants; convergence test results; lattice constants and shear moduli as a function of pressure; PBE-based band structures and density of states; pressure-induced band gap evolution; characteristic band structures with SOC; imaginary part of dielectric function calculated using RPA and BSE; BSE-based optical absorption spectra and frequency-dependent optical reflectivity (PDF)

AUTHOR INFORMATION

Corresponding Author

*E-mail: xin.xi.luo@polyu.edu.hk (X.L.); aphhuang@polyu.edu.hk (H.H.).

Author Contributions

The manuscript was written through contributions of all authors. All authors have given approval to the final version of the manuscript.

Notes

The authors declare no competing financial interests.

ABBREVIATIONS

MHP, metal halide perovskite; NC, nanocrystal; DAC, diamond anvil cell; DFT, density functional theory; SOC, spin-orbit coupling; PAW, projector-augmented wave; LDA, local density approximation; GGA, generalized gradient approximation; PBE, Perdew-Burke-Ernzerhof; PBEsol, PBE revised for solids; VBM, valence band maximum; CBM, conduction band minimum; DFPT, density functional perturbation theory; BSE, Bethe-Salpeter equation; RPA, random phase approximation; DOS, density of state; WM, Wannier-Mott.

REFERENCES

1. Eperon, G. E., et al., Perovskite-perovskite tandem photovoltaics with optimized band gaps. *Science* **2016**, *354*, 861-865.

2. Kojima, A.; Teshima, K.; Shirai, Y.; Miyasaka, T., Organometal Halide Perovskites as Visible-Light Sensitizers for Photovoltaic Cells. *J. Am. Chem. Soc.* **2009**, *131*, 6050-6051.

3. Hodes, G., Perovskite-Based Solar Cells. *Science* **2013**, *342*, 317-318.

4. Kim, H. S., et al., Lead iodide perovskite sensitized all-solid-state submicron thin film mesoscopic solar cell with efficiency exceeding 9%. *Sci. Rep.* **2012**, *2*, 591.

5. Yang, W. S., et al., Iodide management in formamidinium-lead-halide-based perovskite layers for efficient solar cells. *Science* **2017**, *356*, 1376-1379.

6. Eperon, G. E.; Stranks, S. D.; Menelaou, C.; Johnston, M. B.; Herz, L. M.; Snaith, H. J., Formamidinium lead trihalide: a broadly tunable perovskite for efficient planar heterojunction solar cells. *Energ. Environ. Sci.* **2014**, *7*, 982-988.

7. Im, J. H.; Jang, I. H.; Pellet, N.; Gratzel, M.; Park, N. G., Growth of $CH_3NH_3PbI_3$ cuboids with controlled size for high-efficiency perovskite solar cells. *Nat. Nanotechnol.* **2014**, *9*, 927-932.

8. Heo, J. H., et al., Planar $CH_3NH_3PbI_3$ Perovskite Solar Cells with Constant 17.2% Average Power Conversion Efficiency Irrespective of the Scan Rate. *Adv. Mater.* **2015**, *27*, 3424-3430.

9. Kulbak, M.; Gupta, S.; Kedem, N.; Levine, I.; Bendikov, T.; Hodes, G.; Cahen, D., Cesium Enhances Long-Term Stability of Lead Bromide Perovskite-Based Solar Cells. *J. Phys. Chem. Lett.* **2016**, *7*, 167-172.

10.   Protesescu, L.; Yakunin, S.; Bodnarchuk, M. I.; Krieg, F.; Caputo, R.; Hendon, C. H.; Yang, R. X.; Walsh, A.; Kovalenko, M. V., Nanocrystals of Cesium Lead Halide Perovskites (CsPbX$_3$, X = Cl, Br, and I): Novel Optoelectronic Materials Showing Bright Emission with Wide Color Gamut. *Nano Lett.* **2015**, *15*, 3692-3696.

11.   Swarnkar, A.; Chulliyil, R.; Ravi, V. K.; Irfanullah, M.; Chowdhury, A.; Nag, A., Colloidal CsPbBr$_3$ Perovskite Nanocrystals: Luminescence beyond Traditional Quantum Dots. *Angew. Chem. Int. Ed.* **2015**, *54*, 15424-15428.

12.   Li, X. M.; Wu, Y.; Zhang, S. L.; Cai, B.; Gu, Y.; Song, J. Z.; Zeng, H. B., CsPbX$_3$ Quantum Dots for Lighting and Displays: Room-Temperature Synthesis, Photoluminescence Superiorities, Underlying Origins and White Light-Emitting Diodes. *Adv. Funct. Mater.* **2016**, *26*, 2435-2445.

13.   Yantara, N.; Bhaumik, S.; Yan, F.; Sabba, D.; Dewi, H. A.; Mathews, N.; Boix, P. P.; Demir, H. V.; Mhaisalkar, S., Inorganic Halide Perovskites for Efficient Light-Emitting Diodes. *J. Phys. Chem. Lett.* **2015**, *6*, 4360-4364.

14.   Song, J.; Li, J.; Li, X.; Xu, L.; Dong, Y.; Zeng, H., Quantum Dot Light-Emitting Diodes Based on Inorganic Perovskite Cesium Lead Halides (CsPbX$_3$). *Adv. Mater.* **2015**, *27*, 7162-7167.

15.   Wang, Y.; Li, X.; Song, J.; Xiao, L.; Zeng, H.; Sun, H., All-Inorganic Colloidal Perovskite Quantum Dots: A New Class of Lasing Materials with Favorable Characteristics. *Adv. Mater.* **2015**, *27*, 7101-7108.

16.   He, X.; Liu, P.; Zhang, H.; Liao, Q.; Yao, J.; Fu, H., Patterning Multicolored Microdisk Laser Arrays of Cesium Lead Halide Perovskite. *Adv. Mater.* **2017**, *29*, 1604510.

17.   Jellicoe, T. C., et al., Synthesis and Optical Properties of Lead-Free Cesium Tin Halide Perovskite Nanocrystals. *J. Am. Chem. Soc.* **2016**, *138*, 2941-2944.

18.   Akkerman, Q. A.; D'Innocenzo, V.; Accornero, S.; Scarpellini, A.; Petrozza, A.; Prato, M.; Manna, L., Tuning the Optical Properties of Cesium Lead Halide Perovskite Nanocrystals by Anion Exchange Reactions. *J. Am. Chem. Soc.* **2015**, *137*, 10276-10281.

19.   Zhang, X.; Lin, H.; Huang, H.; Reckmeier, C.; Zhang, Y.; Choy, W. C.; Rogach, A. L., Enhancing the Brightness of Cesium Lead Halide Perovskite Nanocrystal Based Green Light-Emitting Devices through the Interface Engineering with Perfluorinated Ionomer. *Nano Lett.* **2016**, *16*, 1415-1420.

20.   Weidman, M. C.; Seitz, M.; Stranks, S. D.; Tisdale, W. A., Highly Tunable Colloidal Perovskite Nanoplatelets through Variable Cation, Metal, and Halide Composition. *ACS Nano* **2016**, *10*, 7830-7839.

21.   Amgar, D.; Stern, A.; Rotem, D.; Porath, D.; Etgar, L., Tunable Length and Optical Properties of $CsPbX_3$ (X = Cl, Br, I) Nanowires with a Few Unit Cells. *Nano Lett.* **2017**, *17*, 1007-1013.

22.   Lu, X., et al., Enhanced Structural Stability and Photo Responsiveness of $CH_3NH_3SnI_3$ Perovskite via Pressure-Induced Amorphization and Recrystallization. *Adv. Mater.* **2016**, *28*, 8663-8668.

23.   Wang, L.; Wang, K.; Zou, B., Pressure-Induced Structural and Optical Properties of Organometal Halide Perovskite-Based Formamidinium Lead Bromide. *J. Phys. Chem. Lett.* **2016**, *7*, 2556-2562.

24.   Wang, L.; Wang, K.; Xiao, G.; Zeng, Q.; Zou, B., Pressure-Induced Structural Evolution and Band Gap Shifts of Organometal Halide Perovskite-Based Methylammonium Lead Chloride. *J. Phys. Chem. Lett.* **2016**, *7*, 5273-5279.

25.   Wang, P., et al., Pressure-Induced Polymorphic, Optical, and Electronic Transitions of Formamidinium Lead Iodide Perovskite. *J. Phys. Chem. Lett.* **2017**, *8*, 2119-2125.

26.   Liu, G.; Kong, L. P.; Gong, J.; Yang, W. G.; Mao, H. K.; Hu, Q. Y.; Liu, Z. X.; Schaller, R. D.; Zhang, D. Z.; Xu, T., Pressure-Induced Bandgap Optimization in Lead-Based Perovskites with Prolonged Carrier Lifetime and Ambient Retainability. *Adv. Funct. Mater.* **2017**, *27*.

27.   Xiao, G.; Cao, Y.; Qi, G.; Wang, L.; Liu, C.; Ma, Z.; Yang, X.; Sui, Y.; Zheng, W.; Zou, B., Pressure Effects on Structure and Optical Properties in Cesium Lead Bromide Perovskite Nanocrystals. *J. Am. Chem. Soc.* **2017**, *139*, 10087-10094.

28.   Zhang, L.; Zeng, Q.; Wang, K., Pressure-Induced Structural and Optical Properties of Inorganic Halide Perovskite $CsPbBr_3$. *J. Phys. Chem. Lett.* **2017**, *8*, 3752-3758.

29.   Yuan, G.; Qin, S.; Wu, X.; Ding, H.; Lu, A., Pressure-induced phase transformation of $CsPbI_3$ by X-ray diffraction and Raman spectroscopy. *Phase Transit.* **2017**, *91*, 38-47.

30.   Jin, H.; Im, J.; Freeman, A. J., Topological insulator phase in halide perovskite structures. *Phys. Rev. B: Condens. Matter Mater. Phys.* **2012**, *86*, 121102.

31.   Kresse, G.; Furthmuller, J., Efficient iterative schemes for ab initio total-energy calculations using a plane-wave basis set. *Phys. Rev. B: Condens. Matter Mater. Phys.* **1996**, *54*, 11169-11186.

32.   Kresse, G.; Furthmuller, J., Efficiency of ab-initio total energy calculations for metals and semiconductors using a plane-wave basis set. *Comput. Mater. Sci.* **1996**, *6*, 15-50.

33.   Blöchl, P. E., Projector augmented-wave method. *Phys. Rev. B: Condens. Matter Mater. Phys.* **1994**, *50*, 17953-17979.

34.   Perdew, J. P.; Burke, K.; Ernzerhof, M., Generalized gradient approximation made simple. *Phys. Rev. Lett.* **1996**, *77*, 3865-3868.

35.   Perdew, J. P.; Ruzsinszky, A.; Csonka, G. I.; Vydrov, O. A.; Scuseria, G. E.; Constantin, L. A.; Zhou, X.; Burke, K., Restoring the density-gradient expansion for exchange in solids and surfaces. *Phys. Rev. Lett.* **2008**, *100*, 136406.

36.   Peng, H.; Yang, Z.-H.; Perdew, J. P.; Sun, J., Versatile van der Waals Density Functional Based on a Meta-Generalized Gradient Approximation. *Phys. Rev. X* **2016**, *6*, 041005.

37.   Monkhorst, H. J.; Pack, J. D., Special Points for Brillouin-Zone Integrations. *Phys. Rev. B: Condens. Matter Mater. Phys.* **1976**, *13*, 5188-5192.

38.   Le Page, Y.; Saxe, P., Symmetry-general least-squares extraction of elastic data for strained materials from *ab initio* calculations of stress. *Phys. Rev. B: Condens. Matter Mater. Phys.* **2002**, *65*, 104104.

39.   Landau, L. D.; Lifshitz, E. M., *Theory of Elasticity, vol. 7*, 1986; Vol. 3, p 109.

40.   Hashin, Z.; Shtrikman, S., A variational approach to the theory of the elastic behaviour of multiphase materials. *J. Mech. Phys. Solids* **1963**, *11*, 127-140.

41.   Grundmann, M., *The Physics of Semiconductors: An Introduction Including Nanophysics and Applications*; Springer, 2015.

42.   Bardeen, J.; Shockley, W., Deformation potentials and mobilities in non-polar crystals. *Phys. Rev.* **1950**, *80*, 72.

43.   Salpeter, E. E.; Bethe, H. A., A Relativistic Equation for Bound-State Problems. *Phys. Rev.* **1951**, *84*, 1232-1242.

44.   Bickers, N. E.; Scalapino, D. J.; White, S. R., Conserving approximations for strongly correlated electron systems: Bethe-Salpeter equation and dynamics for the two-dimensional Hubbard model. *Phys. Rev. Lett.* **1989**, *62*, 961-964.

45.   Dancoff, S. M., Non-Adiabatic Meson Theory of Nuclear Forces. *Phys. Rev.* **1950**, *78*, 382-385.

46.   Philipp, H. R.; Ehrenreich, H., Optical Properties of Semiconductors. *Phys. Rev.* **1963**, *129*, 1550-1560.

47.   Csonka, G. I.; Perdew, J. P.; Ruzsinszky, A.; Philipsen, P. H. T.; Lebègue, S.; Paier, J.; Vydrov, O. A.; Ángyán, J. G., Assessing the performance of recent density functionals for bulk solids. *Phys. Rev. B: Condens. Matter Mater. Phys.* **2009**, *79*, 155107.

48.   Huang, L.-y.; Lambrecht, W. R. L., Electronic band structure, phonons, and exciton binding energies of halide perovskites $CsSnCl_3$, $CsSnBr_3$, and $CsSnI_3$. *Phys. Rev. B: Condens. Matter Mater. Phys.* **2013**, *88*, 165203.

49.   Brgoch, J.; Lehner, A. J.; Chabinyc, M.; Seshadri, R., Ab Initio Calculations of Band Gaps and Absolute Band Positions of Polymorphs of RbPbI$_3$ and CsPbI$_3$: Implications for Main-Group Halide Perovskite Photovoltaics. *J. Phys. Chem. C* **2014**, *118*, 27721-27727.

50.   Kramers, H. A., A general theory of paramagnetic rotation in crystals *Proc. Amsterdam Acad.* **1930**, *33*, 959-972.

51.   Tan, L. Z.; Rappe, A. M., Enhancement of the Bulk Photovoltaic Effect in Topological Insulators. *Phys. Rev. Lett.* **2016**, *116*, 237402.

52.   Sebastian, M.; Peters, J. A.; Stoumpos, C. C.; Im, J.; Kostina, S. S.; Liu, Z.; Kanatzidis, M. G.; Freeman, A. J.; Wessels, B. W., Excitonic emissions and above-band-gap luminescence in the single-crystal perovskite semiconductors CsPbBr$_3$ and CsPbCl$_3$. *Phys. Rev. B: Condens. Matter Mater. Phys.* **2015**, *92*, 235210.

53.   Stoumpos, C. C.; Malliakas, C. D.; Kanatzidis, M. G., Semiconducting tin and lead iodide perovskites with organic cations: phase transitions, high mobilities, and near-infrared photoluminescent properties. *Inorg. Chem.* **2013**, *52*, 9019-9038.

54.   Peedikakkandy, L.; Bhargava, P., Composition dependent optical, structural and photoluminescence characteristics of cesium tin halide perovskites. *RSC Adv.* **2016**, *6*, 19857-19860.

55.   Wiktor, J.; Rothlisberger, U.; Pasquarello, A., Predictive Determination of Band Gaps of Inorganic Halide Perovskites. *J. Phys. Chem. Lett.* **2017**, *8*, 5507-5512.

56. Heyd, J.; Peralta, J. E.; Scuseria, G. E.; Martin, R. L., Energy band gaps and lattice parameters evaluated with the Heyd-Scuseria-Ernzerhof screened hybrid functional. *J. Chem. Phys.* **2005**, *123*, 174101.

57. Shishkin, M.; Kresse, G., Self-consistent GW calculations for semiconductors and insulators. *Phys. Rev. B: Condens. Matter Mater. Phys.* **2007**, *75*, 235102.

58. Morales-García, Á.; Valero, R.; Illas, F., An Empirical, yet Practical Way To Predict the Band Gap in Solids by Using Density Functional Band Structure Calculations. *J. Phys. Chem. C* **2017**, *121*, 18862-18866.

59. Brandt, R. E.; Stevanović, V.; Ginley, D. S.; Buonassisi, T., Identifying defect-tolerant semiconductors with high minority-carrier lifetimes: beyond hybrid lead halide perovskites. *MRS Commun.* **2015**, *5*, 265-275.

60. Manser, J. S.; Christians, J. A.; Kamat, P. V., Intriguing Optoelectronic Properties of Metal Halide Perovskites. *Chem. Rev.* **2016**, *116*, 12956-13008.

61. Yang, J. Y.; Hu, M., Temperature-Induced Large Broadening and Blue Shift in the Electronic Band Structure and Optical Absorption of Methylammonium Lead Iodide Perovskite. *J. Phys. Chem. Lett.* **2017**, *8*, 3720-3725.

Table of Contents (TOC) Graphic